JOURNAL OF AIRCRAFT
Vol. 45, No. 2, March–April 2008

Dynamics of Vortical Flows Induced by Swept-Notched Wings in Aircraft Wake Simulations

L. Szkatula,* R. J. Grant,† and Z. Zouaoui‡
University of Wales,
Wrexham, LL11 2AW, United Kingdom

DOI: 10.2514/1.28947

The motivation behind the present investigations is the alleviation of vortex wake hazard. The influence of wing-tip geometry modifications on the near-field wake behind swept-notched wings is investigated up to 24 span lengths, using computational fluid dynamics. Three-dimensional parallel simulations are run at a chord-based Reynolds number of 5.34×10^4. The effectiveness of notched wing modifications on wake properties is assessed via comparison with conventional and original notched wings. Current results are promising: the tip and flap vortices produced by the swept-notched wings remain distinct and unmerged, unlike those associated with the conventional wing. In all cases, the wakes of the novel wings have circulations and vorticity values that are substantially lower than the original notched wing. Numerical data clearly indicate that such geometrical combinations break apart the concentrated area of streamwise vorticity shed by the wing into three or more less intense regions, significantly reducing the wake strength and induced rolling moment, and affecting the location and merging process of the overall wake system.

Nomenclature

c	=	wing chord
b_{TF}	=	tip-flap vortex separation distance
C_L	=	lift coefficient
C_M	=	induced rolling moment coefficient
C_M*	=	maximum induced rolling moment coefficient
$\mathrm{d}A$	=	cross-sectional area
k	=	turbulent kinetic energy
Re	=	chord-based Reynolds number
r_c	=	vortex center radius
s	=	wing semispan
s_f	=	follower wing semispan
x, y, z	=	Cartesian coordinate system
U	=	upstream velocity
u, v, w	=	flow velocities in x, y, and z directions
y_c, z_c	=	vortex centroid coordinates
Γ	=	vortex strength
ε	=	dissipation rate of turbulent kinetic energy
ω	=	streamwise vorticity

I. Introduction

SINCE the introduction of the Boeing B747, the severity of the wake vortex hazard has been recognized, and the intense worldwide research, started in the late 1970s, has provided a fundamental understanding of wake dynamics, characteristics, and hazards. The wake hazard is further intensified at airports, where aircraft are continually landing and taking off in the vortex wakes of other aircraft. Rolling motion, structural loads, and loss of control, possibly leading to ground impact, may occur during an encounter with a wake, depending on the follower aircraft's position and orientation with respect to the wake [1,2]. To deal with this potential hazard, the Federal Aviation Administration and Civil Aviation Authority have prescribed safe separation distances between successive airline flights at landing and takeoff conditions. Although these separation standards have proven to be effective from a safety point of view they are conservative, empirical, and frequently prescribe distances in excess of the spacing actually required, significantly reducing airport operational capacities and resulting in unnecessary flight delays [3]. With increasing pressure on airport capacity and the forthcoming introduction of the Airbus A380 "super jumbo," the interest in the wake hazard problem has been reawakened [4]. The European Commission emphasized, in their paper *European Aeronautics: A Vision for 2020* [5], the increasing need for new operational concepts and systems that would permit the tracking and consequential elimination of the trailing wake hazard. Unfortunately, the technology to precisely track the vortices under all weather conditions is currently unavailable. Consequently, a considerable amount of research has been directed toward eliminating wake hazards by modifying the aircraft that generate them.

Many alternative ways [6,7], recently reviewed by Rossow [8], have been explored, proposed, and tested to control and alleviate the wake hazard. Some of these wake alleviation devices, such as pulsatile jets and chordwise blowing, were operated in an active manner and were designed to produce momentum/mass injection. These designs were intended to promote the Crow instability. Other concepts, such as splines or wing-tip mounted engines, were intended to force large amounts of turbulence into the vortices. The idea was that additional turbulence would cause the vortices to dissipate. Researchers also reasoned that if the tip vortex core structure could be broken off, the high swirl velocity generated by the vortex system would be reduced. Passive designs such as vertical fins and winglets were considered, for it was reasoned that by adding vertical fins to the wing tips, the vorticity concentration would be distributed in the vertical direction and would no longer contain a small concentrated vortex area [8]. Sikorsky, in search of a means of reducing blade vortex interaction noise for his helicopter designs, discovered in 1973 that a curved cutback tip (also called an ogee tip and defined as a convex curve leading to a concave curve) could reduce the maximum swirl velocity in the wake vortex to about 25% compared with that of a conventional rectangular square-cut tip design [6]. Small-scale smoke experiments also indicated that the ogee shape diffused the rotor blade tip vortex and the following blades thus encountered a weaker vortex field with accompanying

Presented as Paper at the 45th AIAA Aerospace Sciences Meeting , Reno, Nevada, 8–11 January 2007 ; received 20 November 2006; revision received 8 October 2007; accepted for publication 9 October 2007.

*Ph.D. Candidate, Department of Aeronautical Engineering; l.szkatula@newi.ac.uk. AIAA Member.

†Principal Lecturer, Department of Aeronautical Engineering; r.j.grant@newi.ac.uk.

‡Reader, Department of Aeronautical Engineering; z.zouaoui@newi.ac.uk.

benefits. Further flying data confirmed that the strong impulsive noise signature generated by a standard rotor was significantly reduced using the ogee rotor. Unfortunately, the publications regarding the ogee design were essentially devoted to the rotorcraft industry. Other concepts functioned by modifying the lift distribution of the wing to generate a less hazardous wake profile. Betz, indeed, making the assumption that the roll up of the wake began at the wing tip, established in the early 1930s that vortex core diameters can be expected to differ by a factor of 2 and maximum swirl velocities by a factor of 5 between an elliptic and a triangular load distribution, respectively [8–11]. Two such lift distributions were further considered: a saw-tooth wing loading and a tailored wing loading. Using Betz's theory, Rossow [8] showed that a saw-tooth wing loading would generate a vortex sheet that theoretically translates downward as a single system with no concentrated vortices. A tailored wing loading was shown to create large and diffuse vortices that rotate as rigid bodies. Finally, depending on the load distribution, the wake vortex from an aircraft may, even at the start of its life, be very different from that produced by another one. In spite of the large number of designs that were tested, none of them were practically implemented as a solution to the wake hazard. Simply put, some of these alleviation devices did not effectively reduce the wake hazard at near- and far-field regions, and those that did were discarded due to a number of factors including structural and mechanical effects, control complications, and costs.

Because Betz's method made a direct association between the span loading and the roll up of the wake, Graham [12] recently reasoned that it might be possible to generate an optimum span distribution, so that the vortex wake produced is non or less hazardous. Using a "steepest descent" algorithm to locate an optimum wing span loading, Graham [12] demonstrated that significant reductions (20–25%) in the rolling moment induced on a following aircraft could be achieved using an optimal "notched" wing loading. The algorithm employed successively modified a parametric description of the wing loading, starting from a purely elliptical loading until an optimum lift distribution was reached. The "performance" measure was based on the rolling moment induced on a following aircraft encountering the wake. The ultimate and optimum performance was thus associated with a minimum hazard value. His approach further elucidated that the generation of this less hazardous wake was directly connected to a region of negative vorticity, which prevented the merging of the tip and flap vortices. Graham's predictions were later confirmed by experimental wake survey investigations carried out by Park et al. [13,14] in the Cambridge University low-speed towing tank using rectangular wings. Note that the merger of the vortical structures generated behind the wing is important, for it ultimately determines the wake vortex hazard posed to a following aircraft.

Based upon the research conducted by Sikorsky (research work presented by Lee [6], Graham [12], and Park et al.[13,14]), the present analysis aims to gain a better understanding of how the optimal notched wing, when combined with the ogee/triangular wing-tip modifications, can influence the emerging wake structures, dynamics, and interactions of the wake flows. This research also investigates the viability of these novel swept wings in the context of the wake hazard alleviation. Previous research work carried out by the present authors (Szkatula et al.) and Yang [15,16] for rectangular wings have, indeed, demonstrated that such wing modifications strongly affect the flow features and mergers of the trailing wake vortices. The wakes of the rectangular-notched ogee/triangular wings showed a marked decrease in both the circulation (up to 33%) and rolling moment (up to 46%) when compared with those of a rectangular conventional wing.

The approach taken to the work presented in this paper is numerical, based on validated wake data of conventional and notched rectangular wing designs [13–16]. The geometrical characteristics of the novel swept wings and the computational fluid dynamics (CFD) modelling methods are given in Secs. II and III. The wake properties generated by the swept-notched wings are then described in Sec. IV in the form of vorticity contours, circulation, and rolling moments. The paper is concluded (Secs. V and VI) by considering the implications of the results on the wake hazard.

II. Modelling Methods and Computational Approach

A. Wing Geometrical Characteristics

Two sets of half-swept wings (also referred to as sets 1 and 2) with constant cross sections were considered. All wings had swept plan forms (backward sweep angle Λ of 37.5 deg) with cambered plate geometry cross sections (Göttingen 417). The cross-sectional cambers were circular with a radius of curvature of 210 mm, a thickness of 2 mm, and a nose radius of 1 mm. Set 1 included two wing models, referred to as models 1 and 2, representing a high-lift configuration (also known as a swept conventional wing) and a notched wing, respectively (see Fig. 1). Four novel swept-notched wings, referred to as models 3, 4, 5, and 6, were included in set 2 (see Fig. 2). Note that the geometrical characteristics of the notch (depth, width, and location) for wing models 3–6 remained unchanged when compared with wing model 2; only the wing-tip sections were modified. The wing-tip modifications were adopted and subsequently modeled at 50% chord length (denoted hereafter as 50%c), measured from the leading edge and at three spanwise locations, namely, 225, 240, and 261 mm, measured from the wing root. These values correspond to 75% semispan (denoted as 75%s), 80% semispan (denoted as 80%s), and 87% semispan (denoted as 87%s). In addition, two wing-tip geometries were adopted and tested, namely, the triangular wing-tip section (denoted as and abbreviated to Tri) and the ogee wing-tip section (denoted as Sik), as shown in Figs. 3 and 4. To allow the reader to follow the analysis more closely, a specific classification for wing models 3–6 was created, which included the chord position, the wing-tip section used (triangular or ogee), and the location along the span, respectively. For instance, model 3 is referred to as SN50Tri75, which reads "swept-notched wing with triangular wing-tip section adopted at 50% chord length from the leading edge and 75% semispan from the wing root." Models 4–6 are referred to as SN50Sik75, SN50Sik80, and SN50Sik87, respectively.

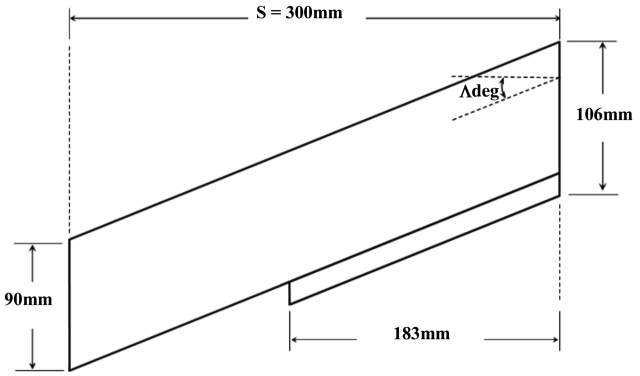

a) Model 1: Reference Wing - Swept Conventional

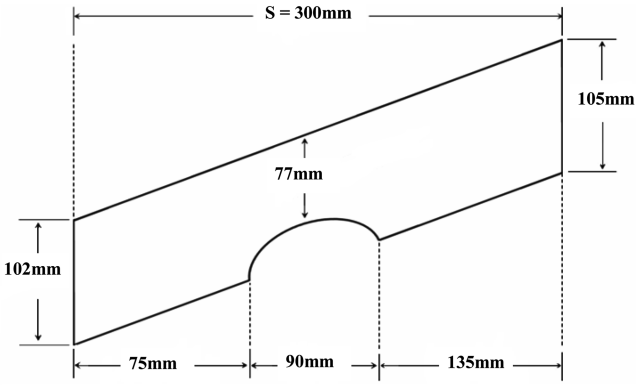

b) Model 2: Reference Wing - Swept Notched

Fig. 1 Wing geometry definition, set 1.

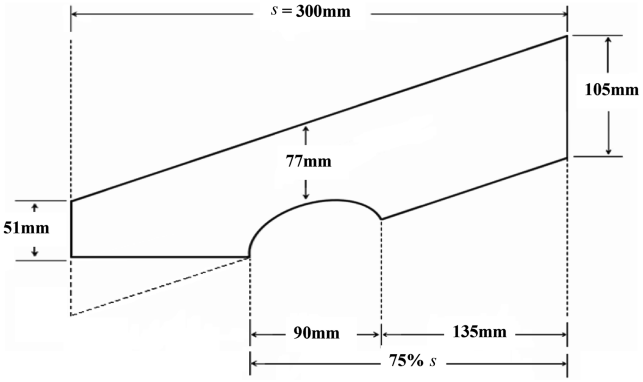

a) Model 3: SN50Tri75

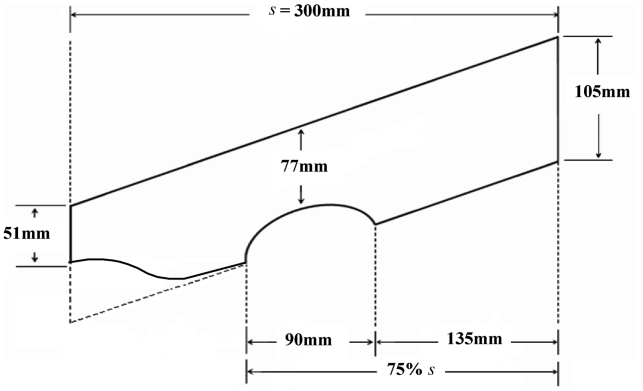

b) Model 4: SN50Sik75

Fig. 2 Wing geometry definition, set 2.

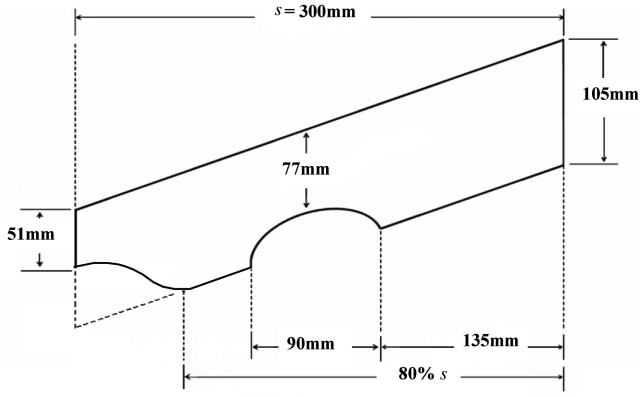

a) Model 5: SN50Sik80

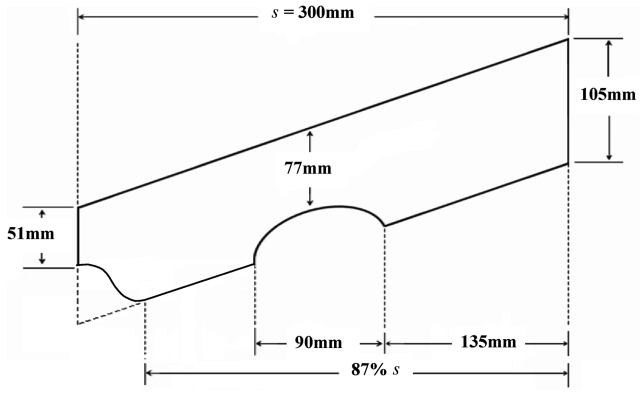

b) Model 6: SN50Sik87

Fig. 3 Wing geometry definition, set 2 (continued).

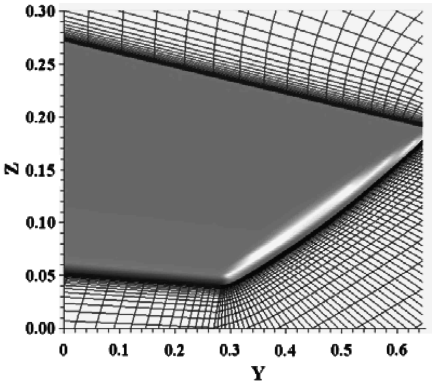

Fig. 4 Computational mesh, grid topology. Detail of the regular structured grid close to the wing-tip surfaces.

The motivation behind the choice of these novel swept wing geometrical designs is a result of three independent research works conducted by Sikorsky (research work presented by Lee [6], Graham [12], and Park et al. [13,14]) and additional work by the present authors and Yang [15,16]. The first two analyses demonstrated that, individually, the ogee and notch geometrical concepts show promise in the context of wake hazard alleviation. Note that these concepts were deemed to be the optimum configurations in each individual test. Sikorsky (research work presented by Lee [6]) demonstrated that with the wing tips acting as generators of intense vortices, applying the convex–concave curve design to a conventional rectangular wing tip reduced the strength of the wakes that were trailed behind the rotor blades. In addition, this advanced shape was observed to diffuse the rotor blade tip vortex, generating a weaker wake field for the following blades, with reduced rotor vibrations and noise signature. The other promising design is the notch concept, developed by Graham [12]. Results have indicated that although the trailing vortices cannot be eliminated, they can be forced to keep their individual structures from the near- to the far-field region, which results in a "safer wake." Graham's investigation also included the variation of the notch depth, width, and spanwise location for rectangular wings. He concluded that the "performance" parameter was relatively insensitive to the depth of the notch in comparison with its location and width. Based upon these two research works, the present authors decided to investigate and evaluate the application of the notch concept combined with the ogee/triangular wing-tip configurations. Note that it was considered that a plain triangular wing-tip section, instead of the elegant ogee curve, could be successful in reducing the strength of the trailed wakes. Finally, according to the results obtained with the rectangular-notched ogee/triangular wings, the first four optimum wing geometries were selected and applied to swept wings; those models correspond to models 3, 4, 5, and 6.

B. Domain Grid

The CFD modelling of the flow is now addressed. GAMBIT© software was used to generate and analyze grids of the novel swept wings during this study. A simplified model of the water tank section ($0.93 \times 1.26 \times 7.69$ m), initially employed for the testing of the experimental rectangular-notched wings [13,14], was virtually created. The outflow boundary was located 24 span lengths downstream from the trailing edge. It should be noted that, to reduce wall interference, the boundaries were kept sufficiently far from the wing models. A *C–H* body fitted grid system using a regular and structured grid containing 4.3×10^6 hexahedral cells was selected to represent the far-field boundaries. A grid resolution study was initially performed to establish a grid independent solution and to determine the size of the grid for which no changes or small changes (<5%) in the accuracy of the computed solutions would be observed. Grid dependency analyses with various near-wall grid lines were performed on vorticity magnitude, total circulation, and merging characteristics at near- and far-field regions [17].

Originally, the grid spacing was relatively coarse on the far-field regions, causing concern that the coarse grid was inadequate for accurately predicting the wake and merging characteristics of the novel wings. As a result, a fine grid was developed from the coarse grid by clustering points to the wings in the chordwise and spanwise directions at the leading and trailing edges (see Fig. 4). Cells were added at the notch and flap extensions to eliminate the coarse grid size in that vicinity. The number of points in the boundary layer was also increased over the entire wing for all wing designs. In addition, the grid density at far-field regions was equal to that of the highly resolved grid made on the near-field regions to capture the complex wake interaction and evolution accurately. Note that a multiblock grid methodology was used to mesh the wing-tip sections of models 5 (SN50Tri75) to 8 (SN50Sik87), allowing one to handle complex geometries and avoiding excessive skewness. The wall adjacent cells were considered to be in the viscous sublayer ($y+ \sim 1$). Finally, particular attention was paid to the mesh quality to maintain a cell skew and aspect ratio below acceptable limits.

C. Computer Requirements and Solution Convergence

The computational simulations were performed using version 6.2 of the finite-volume-based code FLUENT©. Each case was run using either four or eight processors. The numerical model in the present analysis solved the full set of Reynolds-averaged Navier–Stokes (RANS) equations for a three-dimensional incompressible fluid and a steady-state environment. The governing integral equations for the conservation of mass, momentum, and other scalars, such as turbulence, were solved using a segregated solution method. The linearization of the equations was chosen to be implicit in time. The two-equation renormalization group theory (RNG) k–ε turbulence model was used for the present simulations and demonstrated a good overall convergence and robustness. Note that initially the flow simulations were performed with a laminar and Spalart–Allmaras turbulence model. However, the numerical results for the rectangular-notched wings using the RNG k–ε proved to be in better agreement (error percentage inferior to 6%) with the experiments and predicted more accurately the wake dynamics, evolution, and interaction. In addition, the RNG k–ε turbulence model confirmed its ability to maintain coherent and realistic vortex structures downstream of the wing up to 24 span lengths (denoted hereafter as $24s$). It should be noted that, although the k–ε model is a high Reynolds number model, the RNG theory provides an analytically derived differential formula for effective viscosity that accounts for low Reynolds number effects [18–20]. Effective use of this feature does, however, depend on an appropriate treatment of the near-wall region. The near-wall modelling significantly impacts the fidelity of numerical solutions, in as much as walls are the main source of vorticity and turbulence. Therefore, accurate representation of the flow in the near-wall region is key to the successful prediction of the wake characteristics. For the present study, the enhanced-wall treatment was employed, enabling the viscosity-affected region to be resolved with a mesh extending up to the wall, including the viscous sublayer. The Reynolds number based on the chord length was 5.34×10^4, with a freestream velocity of 0.534 ms^{-1}. The angle of attack was set to 0 deg and the flow fluid was modeled as a single component fluid with the properties of water. Convergence to a steady state was generally achieved within approximately 3000 grid cycles, requiring 120–144 CPU hours, depending on the order scheme settings. For stability reasons, an initial solution was first computed with a first-order accuracy. Higher orders (second and third orders) of accuracy were then achieved for flow calculations. Note that these higher-order upwind discretization schemes have the potential to improve spatial accuracy by reducing the effects of numerical diffusion on the flow solution, most significantly for complex three-dimensional flows. Each solution was deemed "converged" when the change in vorticity magnitude and total circulation at the outflow boundary condition over the last 500 iterations was less than 1.0×10^{-4}. Reductions in the residual of at least 6 orders of magnitude were typical.

III. Postprocessing and Data Parameterization

A. Postprocessing Data Collection

Details of the wake flow structures were obtained by means of 44 bounded measurement planes with a spacing of $0.6s$. The first measurement plane was located at $0.3s$ downstream from the trailing edge and the last one at $24s$. Each crossflow plane was normal to the freestream velocity and contained 41×41 data points. The location, size, and strength of the vortical structures were captured at each measurement plane. Data sets are presented in both normalized and dimensional forms to convey practical information about magnitudes and averaged values. Such analyses produce a vast quantity of results; only the most relevant data are presented here. The following methods are used to characterize the vertical structures and investigate their interactions.

B. Vortex Vorticity, Circulation, and Core Radius

The physical vortex properties, such as vorticity, circulation, and centroid locations, are discretized on a Cartesian staggered grid. The strength properties in the wake were measured by means of standard definitions. The vorticity field provided by the FLUENT© postprocessing data control panel is derived from the velocity field and calculated at each cell center. The vorticity is defined as the curl of the velocity V:

$$\omega = \nabla \times \mathrm{V} \tag{1}$$

which can be expressed as

$$\omega = \mathrm{i}\left(\frac{\partial \mathrm{w}}{\partial \mathrm{y}} - \frac{\partial \mathrm{v}}{\partial \mathrm{z}}\right) - \mathrm{j}\left(\frac{\partial \mathrm{w}}{\partial \mathrm{x}} - \frac{\partial \mathrm{u}}{\partial \mathrm{z}}\right) + \mathrm{k}\left(\frac{\partial \mathrm{v}}{\partial \mathrm{x}} - \frac{\partial \mathrm{u}}{\partial \mathrm{y}}\right) \tag{2}$$

The circulation is intimately related to the vorticity and is defined as the line integral of a closed loop in the velocity field. Using a regular orthogonal grid, the circulation of one square cell, Γ_{cell}, at the center, is given by the product of the cell lengths and the sum of the velocity

$$\Gamma_{\mathrm{cell}} = \left(\int_{j,\ell}^{j+1,\ell} \mathrm{vdy} + \int_{j+1,\ell}^{j+1,\ell+1} \mathrm{wdz} + \int_{j+1,\ell+1}^{j,\ell+1} \mathrm{vdy} + \int_{j,\ell+1}^{j,\ell} \mathrm{wdz}\right) \tag{3}$$

The average circulation of a single cell is thus expressed as a function of the average vorticity of the so-considered cell:

$$\Gamma_{\mathrm{cell}} = \mathrm{w}_{\mathrm{cell}} \times (\delta y \times \delta z) \tag{4}$$

Using these equations, the vorticity and circulation of each single cell in the flowfield were estimated. To obtain the total and individual circulations a surface area enclosed by an arbitrary closed loop was first evaluated, according to the vortex contour boundaries, and then discretized into many small elements.

To analyze the structural evolutions of the vortices, the tangential velocity profiles are determined from the in-plane velocity components (v, w), which allow direct determination of the peak tangential velocity and the corresponding core radius r_c. Note that the method employed in the present analysis to evaluate the individual core sizes was to draw a circular contour with radius coincident with the location of a maximum azimuthally averaged tangential velocity for each vortex. This definition is widely used in practice and comes from the observation that the Rankine vortex contains 100% of the circulation of the vortex within the maximum velocity radius. It is noteworthy that real vortical structures are unlike the Rankine vortex and, in fact, a significant amount of vorticity lies outside the core radius. However, this definition of the core radius ultimately benefits from the fact that its measurement is extremely simple when the center of the vortices and velocity field are known. In addition, the estimated error on measured core radii is small provided that many data points are taken for the tangential velocity profiles. Correlations of experimental and numerical results have indeed proven that the error percentage is approximately 1–3%. It should be noted that, locally, erroneous individual circulation values

are also expected to be observed for largely deformed and unwell-defined vortex structures, such as the vortex systems generated by the complex swept-notched triangular and ogee wings.

C. Vortex Centers

Locating the position of each individual vortex center is crucial, as it allows subsequent variables such as vortex separation distance, circulation, and core size to be determined. The vortex centers were given by the locations of the local maxima of $d\Gamma(y)/dy$, where maximum vorticity occurred at the locations of maximum sheet strength. This leads to a direct estimate of the location of the overall vorticity centroids (y_c, z_c)

$$(y_c, z_c) = \frac{1}{\Gamma}\int (yz)\omega dA \tag{5}$$

where dA is the cross-sectional area.

D. Induced Rolling Moment

Previous investigations of wake alleviation concepts have measured the dynamic forces acting on a following aircraft to determine how effective a particular concept was at reducing the wake hazard. What is available in the current analysis is the two-dimensional velocity fields in the wakes of the novel swept wings, from the moment of formation up to $24s$ downstream from the trailing edge. With this information, it is possible to estimate the induced rolling moment that a following imaginary wing might experience as it travels in the wakes of the novel wings. Based on a strip-theory approach and assuming that the follower wing has a constant chord and section lift–curve slope ($a_f = 2\pi$), the rolling moment coefficient is described as

$$C_M(y, z) = -\frac{a_f}{2}\int_{-sf/s}^{sf/s} \frac{w(y_f)}{U_{\infty f}}\frac{y_f}{s} d(y_f/s) \tag{6}$$

where a and s are the lift–curve slope and wing semispan, respectively. The subscript, f, denotes the characteristics of the follower wing. Here, the follower wing is assumed to fly at the same velocity as the generator wing. The worst-case scenario occurs when the coefficient of the rolling moment, C_M, is a maximum. This usually happens when the center of the follower wing lines up at the center of rotation of a vortex. C_M was evaluated at each grid cell and thus a contour plot of the rolling moment coefficient was obtained for each measurement plane. C_M* is the maximum value of C_M in the field and is used as a hazard parameter. The span of the following wing was taken to be $s_f/s = 1$, 0.5, and 0.25 to replicate various aircraft categories flying behind the wing generator. Note that Rossow [8] performed a similar type of analysis.

IV. Rolled-Up Wake: Results and Discussion

A. Flow Visualization—Vorticity Contours

The flow generated within the virtual test section contains all of the phenomena of current interest: the interaction of multiple, distinct corotating and counter-rotating vortices, merger, and the relaxation of the emerging vortical structures. Figures 5–13 show gray-scale contour levels of the vorticity field for wing models defined in sets 1 and 2 at $x/s = 1.2$, 6, and 24, respectively. The dark gray and black contours represent the positive vorticity regions (counterclockwise sense of rotation), whereas the white contours represent the negative vorticity regions (clockwise sense of rotation). Initially, the tip cores are located on the right-hand side of the contour plots, whereas the flap vortices are located on the left-hand side. Note that the crosses are used to distinguish the center locations of each individual vortex or pole structure throughout this section.

The main disparities in the organization of the wake structures generated by the swept wings are primarily observed at measurement planes close to the trailing edge. Figures 5a and 5b show the structure of the wakes generated behind the swept reference wings, models 1 and 2, respectively, at $x/s = 1.2$. Two and three cores (expressed hereafter as *dipole* and *tripole* vortical structures) are initially formed behind the swept conventional and swept-notched wings, respectively. The two cores generated from the outside wing tip and flap end by the swept conventional wing spiral around each other as a consequence of the interaction of their velocity fields. The cores are observed to move slightly apart and then together as this interaction brings them towards merger (see Figs. 7a and 12a). The flap vortex is distorted and broken into small patches of vorticity also referred to as filaments. Parts of these filaments are then wrapped around the strongest tip core and eventually merge, forming a unique vortex system. Merger begins just downstream $x/s = 23.4$ after about one orbit of the vortex pair and occurs over a streamwise distance of about $2c$. Figure 5b shows how the swept-notched wing modifies the flow in a fundamental manner from the swept conventional wing. Model 2 generates three cores: two cores with positive swirling from the wing tip and the flap end, respectively, and one additional counter-rotating core located in between the corotating tip and flap cores. The most prominent feature of the notched generated wake evolution is the nonmerging of the tip and flap vortical structures (see Figs. 7b and 12b); they remain distinct from the first to the last measurement plane. This large asymmetric core of negative region that separates the tip and flap cores at the early stage of the interaction quickly weakens, separates into small patches of vorticity, and wraps around the tip and flap cores (see Fig. 12b). Note that no significant distortions in vortical structures are observed for the swept-notched wing during the interaction of the multiple vortices.

The wake structures formed behind the novel swept wings at $x/s = 1.2$, 6, and 24 are presented in Figs. 6, 11, and 13, respectively. One observes that initially (see Fig. 6) four poles (expressed hereafter as *quadrupole structures*) are formed behind the novel swept wings defined in set 2. Close-up views indeed reveal that the complex tip core structure of each wing model included in set 2 is initially split into two small cores. These "addition" cores, which are attached to the main tip core structure, are also referred to as "subvortices." Eventually, as the wake evolves downstream, the tip-addition vortex structures rotate in a counterclockwise direction and merge. The tip-addition dipole structures initially observed move toward each other, accelerating the mixing of the tip core structures and expelling weak

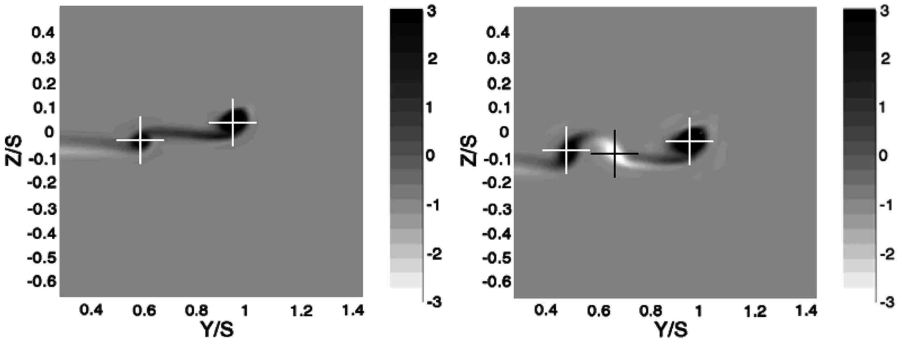

Fig. 5 Vorticity fields ws/U at $x/s = 1.2$: a) wing model 1, and b) wing model 2.

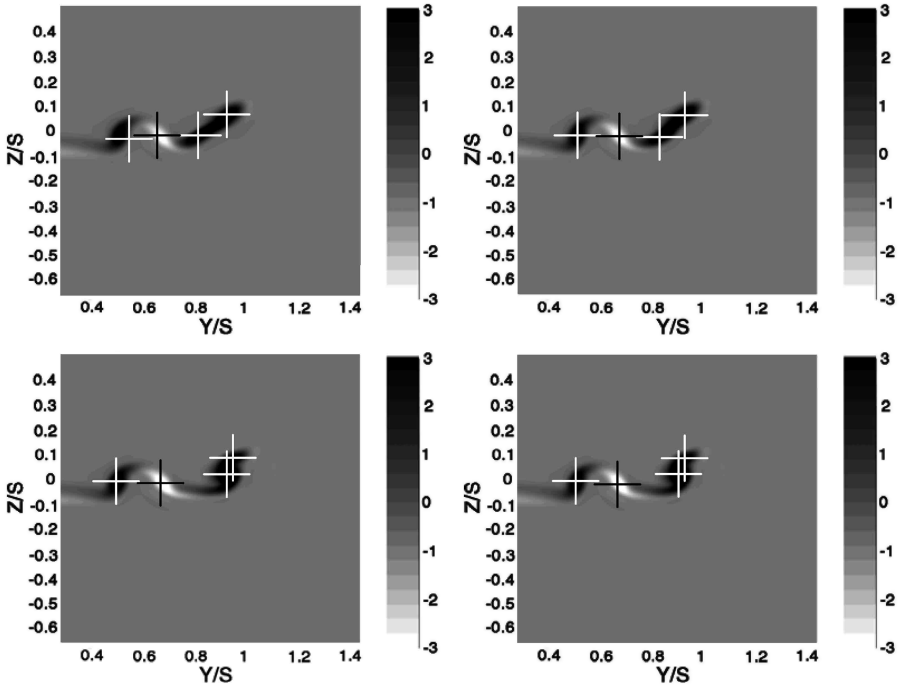

Fig. 6 Effect of wing-tip geometries on the rolled-up vorticity field ws/U at $x/s = 1.2$: a) model 3 (SN50Tri75), b) model 4 (SN50Sik75), c) model 5 (SN50Sik80), and d) model 6 (SN50Sik87).

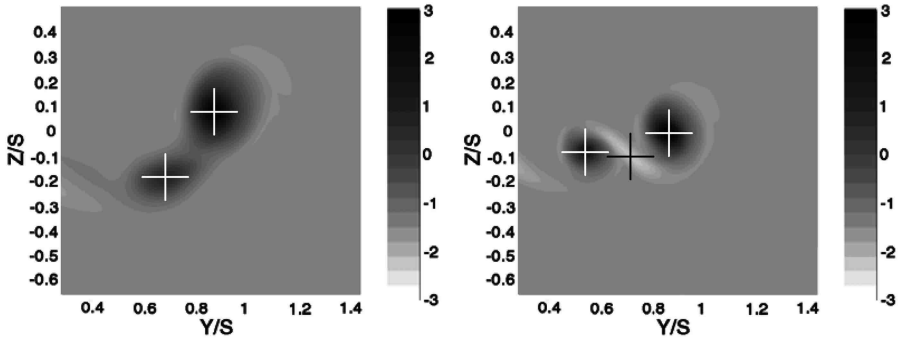

Fig. 7 Vorticity fields ws/U at $x/s = 6$: a) wing model 1, and b) wing model 2.

filamentary debris that seem to surround the emerging tip structures. The organization of these quadrupole structures at near-field regions suggests a strong dependence on wing-tip modifications. The associated downstream wakes (see Figs. 8, 9, 11, and 13) suggest that two merger processes occur between the main tip and the addition vortex structures; these two merger processes are referred to as merger process A and B throughout the remainder of this section. It is hypothesized that merger process B occurs for the wing-tip sections modeled at 80 and 87%s (models 5 and 6), whereas merger process A is defined for the wing-tip sections modeled at 75%s (models 3 and 4). These two merger mechanisms are primarily influenced by the separation distance tip-addition cores, b_{TA}, and the vorticity strength ratio, $\gamma = \omega_{\mathrm{addition}}/\omega_{\mathrm{tip}}$, of the main tip and addition structures. As illustrated in Fig. 9, the wing-tip sections modeled at 80 and 87%s generate weak subvortices, which quickly drift into the main tip structures. In contrast, as the wing-tip sections are modeled close to 75%s, stronger addition vortices are created at the expense of the main tip structures (see Fig. 8). Note that the tip vortex structures become less axisymmetric as the spanwise locations of the wing-tip modifications are moved inboard toward 75%s. As a result, the interaction and merger mechanism between the tip-addition vortical structures is prolonged. As the convective and merging processes are completed, the emerged tip structures are pushed to a great extent toward the flap vortex, which suggests that a greater reduction in the tip-flap vortex separation distance (denoted hereafter as b_{TF}) when compared with the baseline case, wing model 2, is associated with the wing-tip sections modeled at 75%s as opposed to the wing-tip sections modeled at 80 and 87%s. These remarks are further observed in the light of the tip-flap core trajectories (see Fig. 10). Despite the fact that the effects of the addition vortex structures on the main tip vortex structures and on the overall wake evolution mechanism are not yet fully understood and characterized, the fundamental effects of the wing-tip modifications appear to be similar to the rectangular-notched wings, that is, a weakening and an initial shift in the tip vortex. Figures 11 and 13 provide further insights into the wake evolutions of the novel swept wing defined in set 2, and illustrate how the tripole and quadrupole vortex structures have rolled up between $x/s = 1.2$ and $x/s = 6$. The quadrupole vortex structures observed earlier in Fig. 6 for the wing models defined in set 2 are now reorganized into tripole vortex structures, in which the outer cores rotates into an opposite direction when compared with the center core, that is, the negative region. The dipole tip-addition structures, initially observed, have moved toward each other and merged. In each case, the emerging tip vortex structures are observed to be stronger and larger in comparison with the flap vortex structures. Note that the negative region initially located in between the tip and flap vortex structures is confined to a narrow region located underneath the tip core, and flow evolutions eventually reveal that it becomes stretched and orbits around the emerging tip structure.

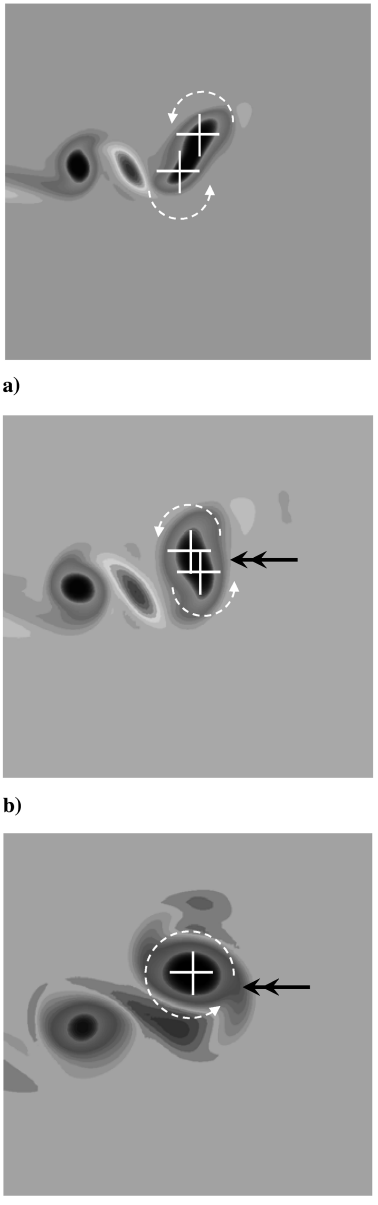

Fig. 8 Merging process A for wing-tip sections modeled at 75%s: a) $x/s = 1.8$, b) $x/s = 3$, and c) $x/s = 5.5$.

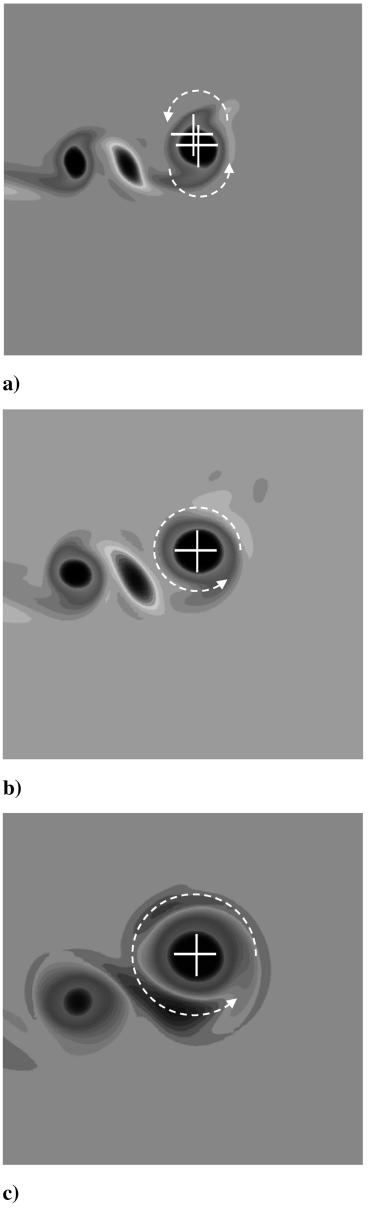

Fig. 9 Merging process B for wing-tip sections modeled at 80 and 87%s: a) $x/s = 1.8$, b) $x/s = 3$, and c) $x/s = 5.5$.

B. Vortex Core Spacing

The corresponding vortex separation distances for the wing models defined in sets 1 and 2 are shown in Fig. 14. Spacing values equal to 0.37 and 0.46s are initially recorded for the swept conventional and swept-notched wings, respectively. As observed earlier, the swept conventional wing shows the merging of its two primary cores, namely, the tip and flap vortices. Note that the completion of the merging process of the tip and flap vortices generated by the swept conventional wing is delayed (completed at $x/s = 23.4$) when compared with the rectangular conventional wing (completed at $x/s = 16.2$). This is mostly explained by the difference in the flap-to-tip vortex strength ratio obtained between the two wing models. Because $|\Gamma_{0f}/\Gamma_{0t}|$ is larger for the swept conventional wing than for the rectangular conventional wing, the flap and tip vortices trace out paths that have larger radii of curvature; hence, the merger occurs later in the case of the swept conventional wing. The merger mechanism observed for the swept conventional wing is analogous to the three-stage merger process described by Cerretelli and Williamson [21] and Leweke et al. [22]. The first period, also identified as the diffusive stage, is defined at interval $x/s = [0; 21]$; the separation distance is observed to remain essentially constant. As the flap structure becomes highly stretched and noticeably deformed, the tip and flap vortex centers are pushed toward one another, causing a rapid linear reduction in vortex separation distance. These observations mark the convective period and are observed at interval $x/s = [21; 23.4]$. Eventually, the tip-flap dipole structure rapidly merges into a single axisymmetrical structure, leaving thin filaments spiralling around the core. Note that the core growth is well sustained after the completion of the merger process (see Table 1). As opposed to the evolution depicted for the swept conventional wing, the swept-notched wing shows no significant decrease in separation distances and hence no merging process between the tip and the flap vortices. This suggests that the central vorticity region, initially located in between the tip and flap vortices, is accountable for the nonmerging of the tip-flap dipole structure. Two primary stages are identified in the spacing evolution of the swept-notched wing. The first period, included at period interval $x/s = [0.9–5]$, is described herein as the first diffusive stage, as it resembles the first stage observed for the swept conventional wing. The convective stage is nonexistent for the swept-notched wing; instead, the spacing between the tip and flap vortices increases slowly, but steadily, until 24s. An increase of 17.5% (24% for the rectangular swept-notched wing) is achieved in vortex spacing for

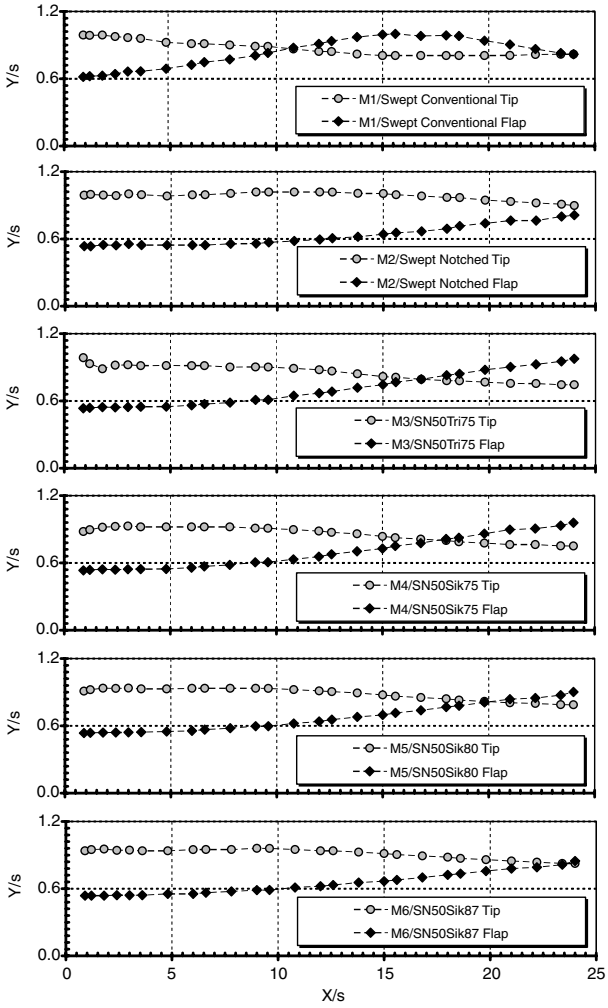

Fig. 10 Vortex core trajectories in the x–y plane.

the swept-notched wing from the first to the last measurement plane. Note that because the analysis of Park et al. [13,14] presents the first knowledge of increasing vortex spacing in a system of two corotating vortices in the literature, very few comments can be made regarding the characteristics of this second "diffusive stage."

Figure 14 also reveals that the novel swept wings' spacing evolutions (set 2) are analogous to the second reference model, the swept-notched wing. The tip and flap vortices stay visibly apart with no merger occurring within the measurement period. Data indicates that model 6 (SN50Sik87) produces the highest separation distance, after reference wing model 2 (swept notched), at all measurement planes, whereas model 3 (SN50Tri75) is observed to produce the lowest tip-flap core spacing. Varying the spanwise wing-tip locations correspondingly increases the spacing values and delays the merger process; spacing values of 0.42, 0.51, and 0.52s are recorded for models 4 (SN50Sik75), 5 (SN50Sik80), and 6 (SN50Sik87), respectively, at $x/s = 24$. However, it should be noted that the variation in vortex spacing is not linear. Substituting the ogee wing-tip section of model 4 (SN50Sik75) for the triangular wing-tip section of model 3 (SN50Tri75) decreases the vortex spacing by an average value of 6%.

C. Core Trajectories and Core Radius

Further insights into the evolution of the flow for sets 1 and 2 are obtained from visualizing the core trajectories themselves (see Figs. 15–17). Note that the thin black lines denote the position of the tip vortices, whereas the gray lines illustrate the flap vortex positions. The centroidal locations of the distinct vortices identifiable in Figs. 5–13 are listed in Tables 1 and 2. Also given are the tip core radii at similar streamwise locations.

The overall orbital evolution observed for the swept conventional wing is very similar to the one observed for the rectangular conventional wing [15,16], as shown in Fig. 15. At the start of the evolution, the tip-flap dipole structure steadily orbits around the overall centroid of the flowfield in a counterclockwise manner. Once the initial roll up is completed, the flap vortex is observed to orbit around the tip vortex with an increasing radius of curvature before mixing with the tip vortex. As the merging time approaches, the dipole structure shows a more pronounced spiralling in while its radius of curvature decreases rapidly. The flap core simply drifts downwards and toward the tip core, slowly approaching one another

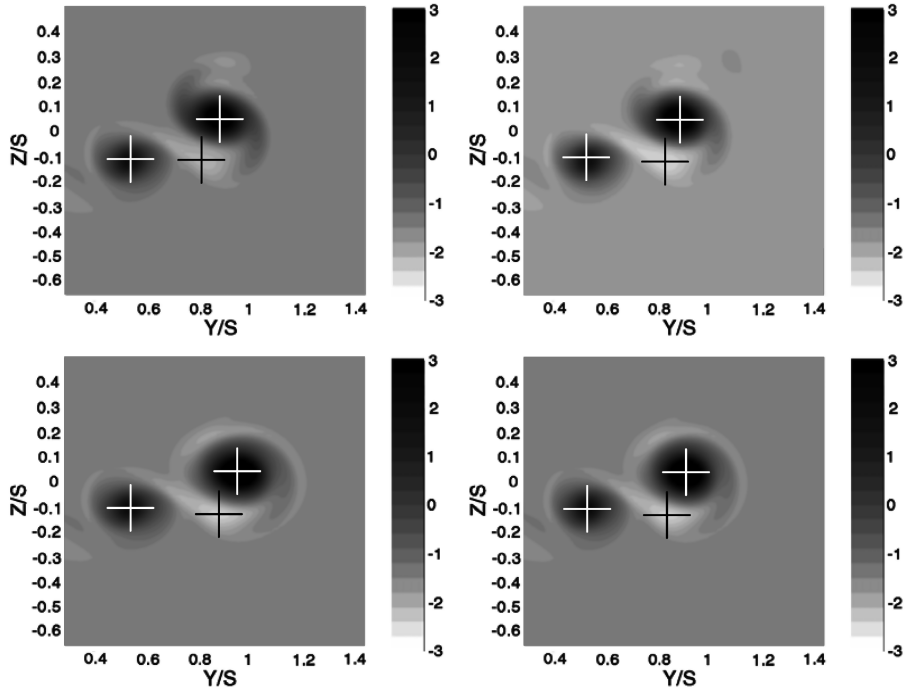

Fig. 11 Effect of wing-tip geometries on the rolled-up vorticity field ws/U at $x/s = 6$: a) model 3 (SN50Tri75), b) model 4 (SN50Sik75), c) model 5 (SN50Sik80), and d) model 6 (SN50Sik87).

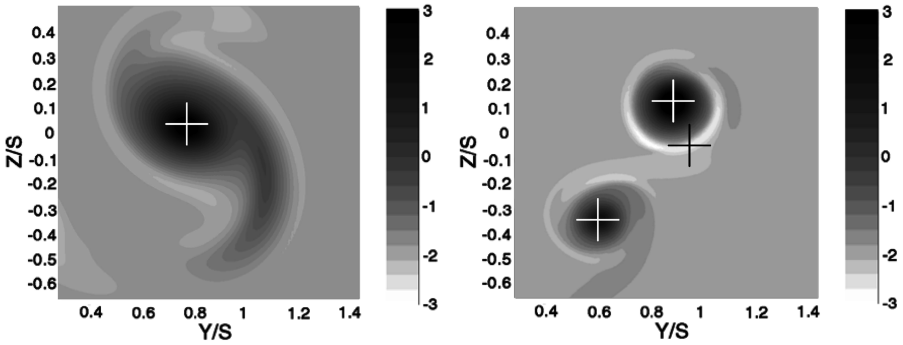

Fig. 12 Vorticity fields ws/U at $x/s = 24$: a) wing model 1, and b) wing model 2.

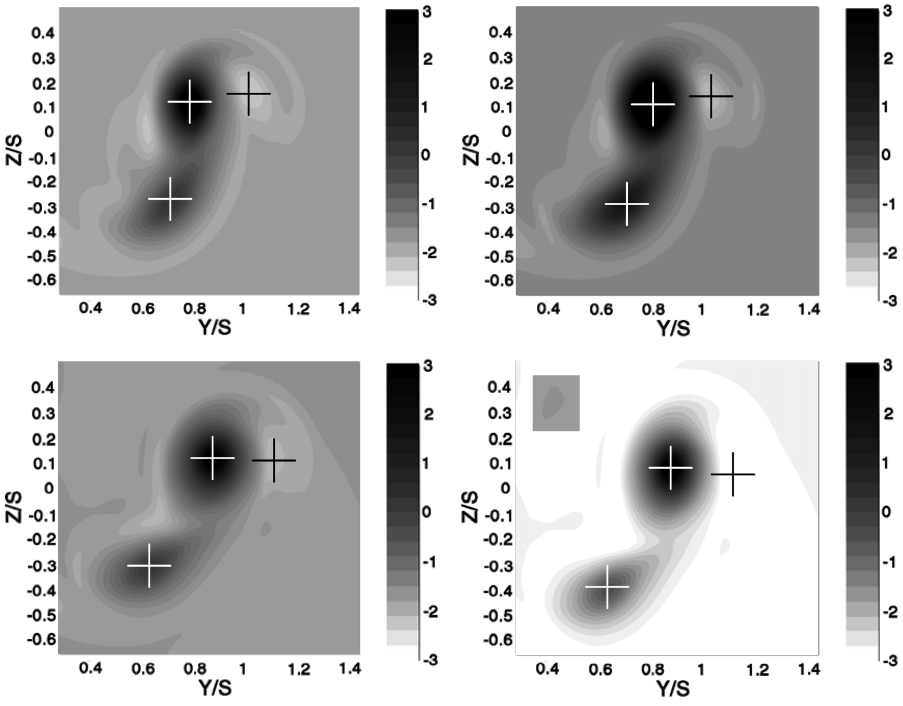

Fig. 13 Effect of wing-tip geometries on the rolled-up vorticity field ws/U at $x/s = 24$: a) model 3 (SN50Tri75), b) model 4 (SN50Sik75), c) model 5 (SN50Sik80), and d) model 6 (SN50Sik87).

and eventually merging, leaving a monopole structure. As the merging process is completed, the long-time evolution is finally described by the trajectories of the overall centroid (see Table 1). As the merger is completed, the emerging core continues its vertical descent. Note that the rate at which the dipole structure of the swept conventional wing rotates is slower than the rate reported for the rectangular conventional wing [15,16]. This confirms the initial increase in separation distance and the subsequent slower decay observed in Fig. 14. The merger is completed within one orbit around the centroid, as observed by Chen et al. [23]. Figure 16 and Table 1 also confirm that no merger occurs for the swept-notched wing. Steady circular paths are observed for the tip-flap dipole structures up to $x/s = 24$.

The core trajectories of the novel wings defined in set 2 (see Fig. 17 and Table 2) show a similar behavior to the core trajectories of the swept-notched wing in that no mergers occur between the tip and flap vortices at any time, and the tip-flap dipole structures trace out circular arcs associated with varying radii of curvature and orbital velocities. Again this is explained by the difference in the flap-to-tip vortex strength ratio obtained between the wing models. Although

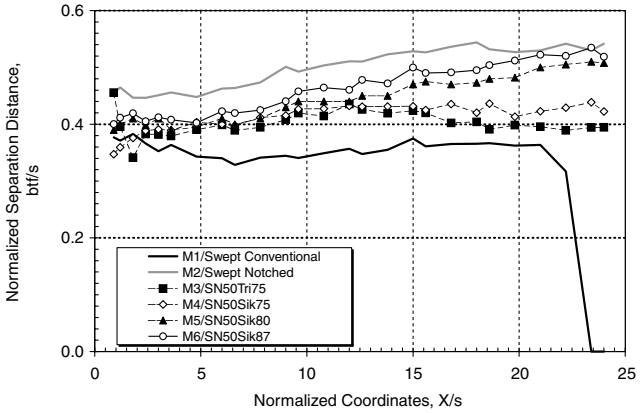

Fig. 14 Evolution of vortex separation distances along normalized axial coordinates for wing models defined in sets 1 and 2.

Table 1 Vortex characteristics for wing models defined in set 1: vortex centroids and core radius

Plan x/s	Model 1 (swept conventional)			Model 2 (swept notched)		
	y_c/s	z_c/s	r_c/s	y_c/s	z_c/s	r_c/s
1.2	0.854	−0.0003	0.0429	0.841	−0.0009	0.0455
6	0.839	−0.0412	0.1361	0.852	−0.0332	0.1301
12	0.867	−0.0553	0.1405	0.885	−0.0361	0.1287
24	0.818	−0.0347	0.1708	0.870	−0.0522	0.1493

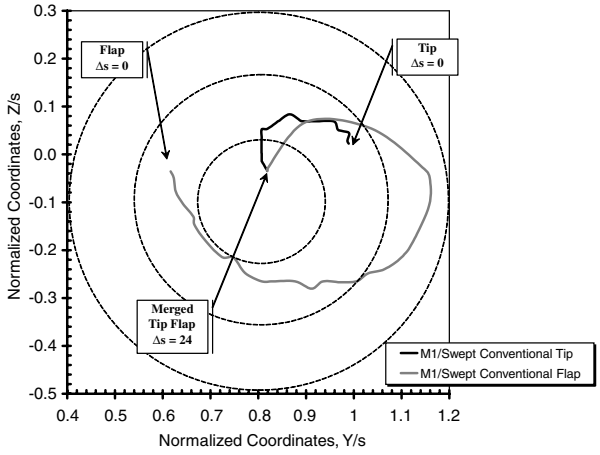

Fig. 15 Two-dimensional core trajectories along normalized coordinates for the swept conventional wing (model 1).

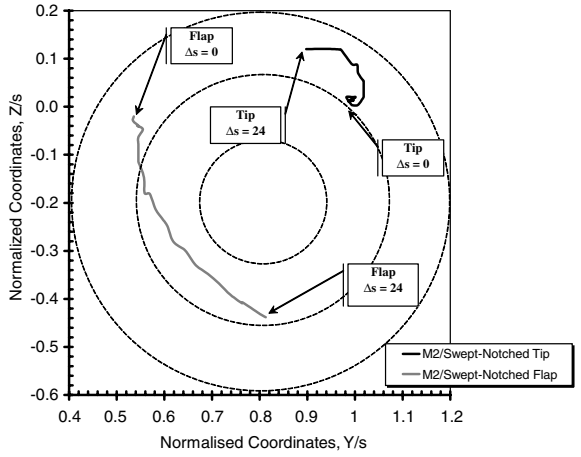

Fig. 16 Two-dimensional core trajectories along normalized coordinates for the swept-notched wing (model 2).

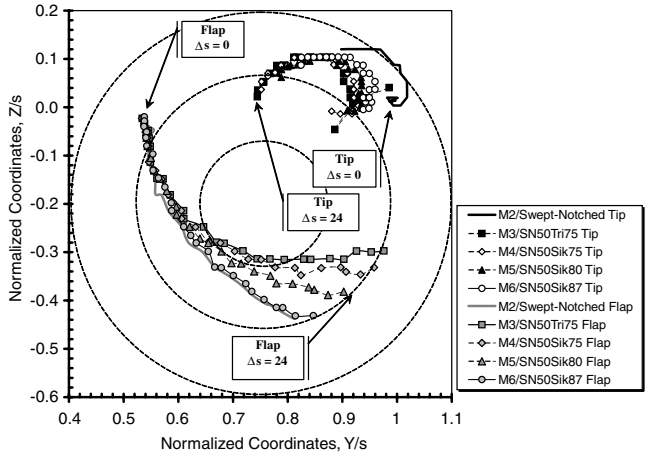

Fig. 17 Effect of wing-tip modifications (wing models defined in set 2) on Two-dimensional core trajectories.

the flap vortex starting locations appear to be almost identical to all set 2 wing models, one finds an inboard shift associated with the initial tip vortex locations ($\Delta s = 0$) when compared with the baseline case model 2 (swept notched). These differences observed in initial tip locations are believed to be related to the subvortices or addition vortices identified at the top extremity of the tip vortices (see Figs. 5 and 6). One interesting result is that the tip vortices of the wing models defined in set 2 have a noticeably rapid descent after their initial roll up, a feature that is not observed with the swept-notched wing. The tip trajectories are observed to straighten out at the end of the record, moving almost parallel to the overall centroid movement. These observations are primarily observed for models 3 (SN50Tri75), 4 (SN50Sik75), and 5 (SN50Sik80), as wing model 6 (SN50Sik87) tends to resemble the reference wing model, model 2 (swept notched). Note that the flap vortex trajectories of the wing models defined in set 2 appear to be much steadier than their respective tip vortices. The tip core radius evolutions, presented in Tables 1 and 2, are independent of the wing-tip geometries; no clear monotonic increases or decreases are observed as the wing tips are modeled from 75 to 100%s. Relocating the ogee wing-tip sections from 75 to 87%s leads to a proportional rise in the radius of curvature and drop in orbital velocities, respectively. The cores induced by model 6 (SN50Sik87) are further away from each other, clearly indicating a larger radius of curvature, a lower orbital speed, and a greater separation distance throughout the interaction when compared with wing model 4 (SN50Sik75). In contrast, the triangular wing-tip section of model 3 (SN50Tri75) reduces the radius of curvature and increases the associated orbital velocity when a comparison is made with the ogee wing-tip section of model 4 (SN50Sik75).

D. Circulation Fields

The individual and global circulation values of wing model sets 1 and 2, given in Figs. 18–21, undoubtedly provide additional details not yet discussed. As observed for the rectangular conventional wing [15,16], the tip vortex circulation of the swept conventional wing remains essentially constant during the diffusive stage. As the merging time approaches, the tip circulation of wing model 1 is observed to suddenly increase. In contrast, the tip circulation of the swept-notched wing is almost constant throughout the measurement period. However, one would note that the tip circulation values of the swept-notched wing seem to follow a monotonic decrease throughout the measurement planes. A possible explanation for this reduction is that the tip circulation data collected are contaminated by the initial subvortices and negative region patches that are observed to enter and/or leave the boundary region of the tip vortex. Note that these small patches of vorticity are extremely difficult to localize and identify. The variations in total circulation for the wing models defined in set 1 are plotted in Fig. 19. Most of the observations already described for the tip circulation variations can be reproduced for the global circulation evolutions. Note, in particular, the decrease in mean total circulation values for the swept-notched wing.

The variations of individual and total circulations through time for the novel swept wings tested in set 2 are presented in Figs. 20 and 21. Generally, significant oscillations in tip circulation evolutions are initially recorded at interval $x/s = [0; 3]$. These variations in circulations are attributed to the subvortices or additional vortices initially created in the vicinity of the tip vortical structures, which introduce noticeable deformations in the tip core contours and errors

Table 2 Vortex characteristics for wing models defined in set 2: vortex centroids and core radius

Plan x/s	Model 3 (SN50Tri75)			Model 4 (SN50Sik75)			Model 5 (SN50Sik80)			Model 6 (SN50Sik87)		
	y_c/s	z_c/s	r_c/s	y_c/s	z_c/s	r_c/s	y_c/s	z_c/s	r_c/s	y_c/s	z_c/s	r_c/s
1.2	0.702	−0.0140	0.0433	0.733	−0.0227	0.0442	0.738	−0.0191	0.0423	0.743	−0.0155	0.0400
6	0.798	−0.0235	0.1114	0.800	−0.0192	0.1018	0.809	−0.0246	0.0981	0.818	−0.0300	0.0937
12	0.796	−0.0468	0.1051	0.795	−0.0551	0.1122	0.813	−0.0492	0.1161	0.831	−0.0432	0.1210
24	0.835	−0.1029	0.1619	0.835	−0.1122	0.1624	0.834	−0.1048	0.1643	0.833	−0.0974	0.1665

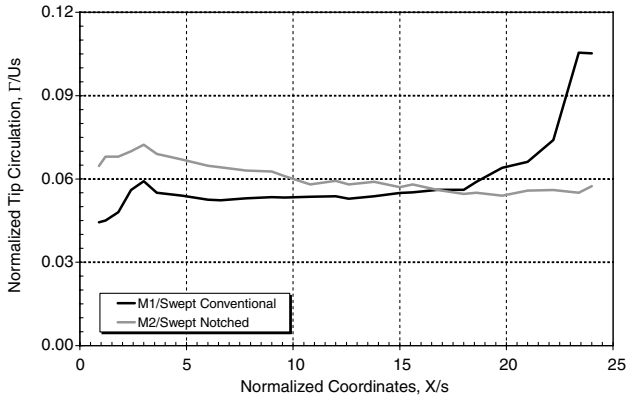

Fig. 18 Normalized individual circulations for wing models defined in set 1.

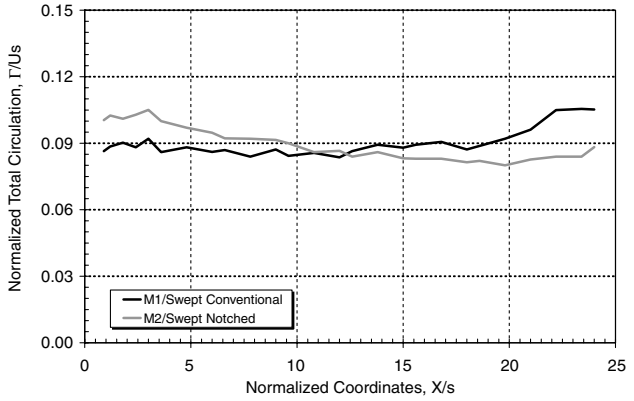

Fig. 19 Normalized total circulation for wing models defined in set 1.

in individual circulation calculations. As the tip vortices start to roll up ($x/s > 3$), the circulations values visibly settle. Note, however, that monotonic decreases in tip and total circulations are visible up to the last measurement plane for all wing models included in set 2. These reductions in circulations are attributed to the wrapping of the negative region around the tip vortex; negative vorticity patches are seen entering the boundary of the tip vortex, introducing once again errors in circulation estimations. One can certainly note the persistence of the negative vorticity patch around the tip vortex and the shedding of filaments at the outer boundaries of the cores. Figures 20 and 21 undoubtedly suggest that the tip and total circulations produced by the swept novel wings defined in set 2 are reduced when compared with the swept-notched reference wing (model 2). The lowest mean tip and total circulations correspond to the triangular and ogee wing-tip sections modeled at 75%s (models 3 and 4). One also finds an overall decrease associated with the wing-tip spanwise locations. These proportions for wing models 3 (SN50Tri75), 4 (SN50Sik75), 5 (SN50Sik80), and 6 (SN50Sik87)

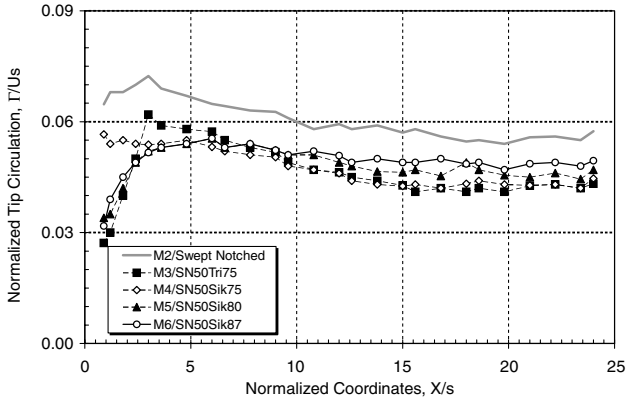

Fig. 20 Normalized individual circulations for wing models defined in set 2.

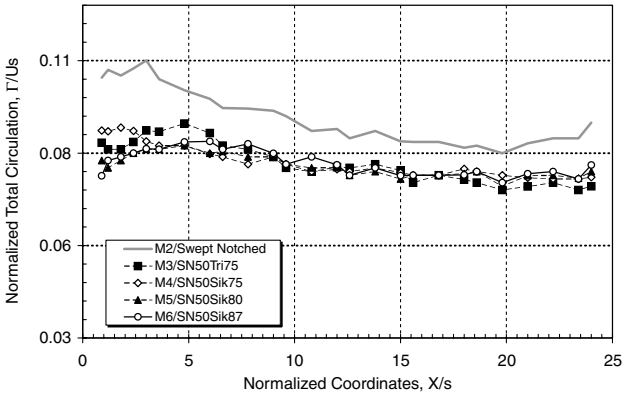

Fig. 21 Normalized total circulation for wing models defined in set 2.

are 30, 27, 19, and 16, respectively. The wing-tip sections located at 75%s appear slightly more efficient in reducing tip circulation, generally achieving larger increments than the wing-tip sections modeled at 80 and 87%s. Turning to Fig. 21, the mean total circulations for the wing models defined in set 2 are lowered by values ranging from 13% [model 6 (SN50Sik87)] to 20% [model 3 (SN50Tri75)] when compared with the swept-notched reference wing. A rise in mean total circulation equal to 3% is recorded between the triangular wing-tip section of wing model 3 (SN50Tri75) and the ogee wing-tip of wing model 4 (SN50Sik75).

E. Induced Rolling Moment

The wakes generated by the novel swept wings are markedly different from the wakes of the reference wings, models 1 and 2. Given these characteristics, the question naturally arises as to how effective the novel swept-notched wings are at reducing the induced rolling moment. To analyze how the rolling moment varies with x/s, the variable C_M* is calculated according to Eq. (6) at various downstream locations. Figures 22–24 show the evolutions of C_M* for follower wings $s_f/s = 1$, 0.5, and 0.25. The evolutions are presented for models 3 (SN50Tri75) to 5 (SN50Sik80), for they are deemed to represent the optimum swept-notched wing configurations and are compared with the swept conventional and swept-notched wings. Note, however, that because the wings in these simulations generate unequal amounts of lift, a more accurate comparison is made by nondimensionalizing the rolling moment coefficients by the respective lift coefficients of the wings.

As one might anticipate, the rolling moment coefficients imposed by the leading wings on the follower wings depend on the downstream position (x/s) and size (s_f/s) of the following wings. As illustrated in Figs. 22–24, a smaller following wing ($s_f/s = 0.5$ and 0.25) shows larger maximum rolling moment coefficients. Smaller wings also experience a larger variation in C_M* values through time. For larger following wings ($s_f/s = 1$ and 0.5), the C_M* values

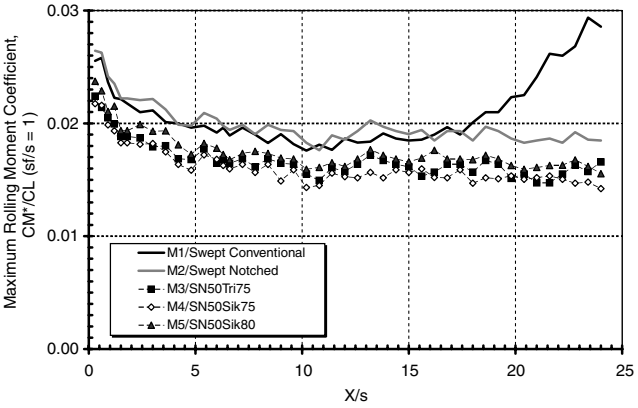

Fig. 22 Normalized maximum rolling moment coefficient C_M*/C_L as functions of downstream locations for a follower wing span $s_f/s = 1$.

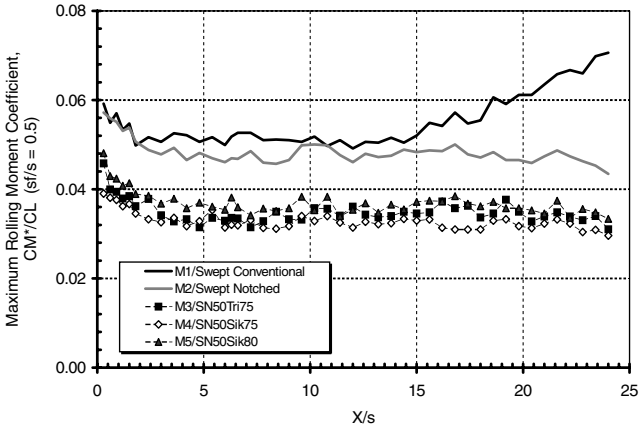

Fig. 23 Normalized maximum rolling moment coefficient C_M*/C_L as functions of downstream locations for a follower wing span $s_f/s = 0.5$.

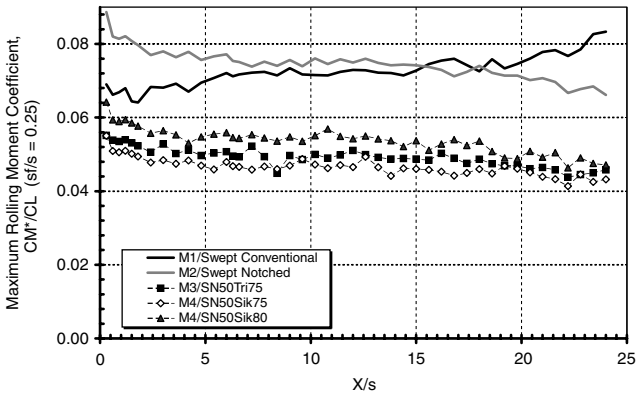

Fig. 24 Normalized maximum rolling moment coefficient C_M*/C_L as functions of downstream locations for a follower wing span $s_f/s = 0.25$.

exhibit a smaller decay over the 24 span measurements. Thus, the wake is just as hazardous to the follower wing at $0s$ as it is at $24s$. One may observe that before $x/s = 20$, the C_M*/C_L values of the swept conventional wing undergo a sudden increase. This is due to the merging process. Similar behavior has been observed in the experimental data [13,14] and simulations of the rectangular conventional wing [15–17]. It was observed that as the merging process is completed, the rolling moment coefficient decreases substantially and continues to decay with time. As demonstrated for the swept conventional wing, the C_M*/C_L values of the swept-notched wing continually decrease from the first to the last measurement plane for all follower wings. By 24 spans, the C_M*/C_L values have decreased by an averaged value of 27% from their initial value. However, one would note that the rolling moment coefficient induced by the swept-notched wing on the follower wing $s_f/s = 0.25$ (see Fig. 24) is higher than the rolling moment coefficient induced by the swept conventional wing. This implies that the swept-notched wing may initially produce a greater region of wake hazard. The reason for this increase in rolling moment is believed to be due to the fact that the swept-notched wing exhibits tighter cores with larger velocities. As a consequence, the smaller wing ($s_f/s = 0.25$) experiences a stronger rolling moment behind the swept-notched wing than behind the swept conventional wing through most of the measurement planes. Again, similar behavior was observed for the rectangular conventional wing [13,14,17]. Experimental data showed that, at further measurement planes ($x/s > 24$), the rolling moment induced in the wake of the rectangular-notched wing was reduced by 13% when compared with the rectangular conventional wing. This is also observed in the present simulations; the rolling moment coefficients of the swept-notched wing drop below the value for the swept conventional wing at $x/s > 18$.

The C_M*/C_L evolutions of the novel swept-notched wings defined in set 2 resemble the evolution of the reference wing, model 2, in that the C_M* values continuously decrease from the first to the last measurement plane. By $24s$, the rolling moment coefficients have decreased by an averaged value of 27% from their initial values. The reason for this reduction in C_M* values is believed to be due to the changes in the tip-flap pair's orientation. Initially, the tip and flap vortices are horizontally aligned and, therefore, impart a larger rolling moment on the following wing. At later measurement planes ($x/s \sim 15$), the vortices are vertically aligned and the corresponding rolling moment coefficients are less. Note, however, that the C_M*/C_L values of the novel swept-notched wings are less than those of the swept-notched wing at all measurement planes and for all follower wing spans ($s_f/s = 1$, 0.5, and 0.25). The novel swept wings show an average 15% ($s_f/s = 1$), 26% ($s_f/s = 0.5$), and 32% ($s_f/s = 0.25$) lower values of C_M*/C_L when compared with the swept-notched wing (model 2). The ogee wing-tip section of model 4 (SN50Sik75) presents the greatest reduction in rolling moment, in which C_M*/C_L is 20% ($s_f/s = 1$), 32% ($s_f/s = 0.5$), and 36% ($s_f/s = 0.25$) less than the average value for the swept-notched wing (model 2). These reductions in the rolling moment coefficient represent notable improvements and confirm that the novel swept-notched wings generate wakes that are "safer" than those induced by the swept conventional and swept-notched wings.

V. Design Issues

As with many of the proposed concepts for reducing the wake hazard, the swept-notched wings come with their own set of challenges. The crucial one is that of lift. By controlling the lift distribution and hence the vortical structures, the lift on the wings is reduced. During landing, the reduction in lift would not be a problem because the plane is decelerating. However, during takeoff and cruise conditions, the reduction in lift would call for higher engine thrust.

Despite these challenges, the novel wing concepts do possess several advantages. The first is that it is completely passive. The notched-ogee wing concept functions by simply placing oppositely signed vortices (negative vorticity region) inboard of the tip vortices and using their presence to keep the coherence of the wake (long-term separation of the tip and flap vortical structures) while reducing the strength of the tip vortex. Note that, because no oscillation flaps or pulsed jets are required, there should be no concerns of degraded passenger comfort as is likely to be the case in wing concepts that periodically vary the lift distribution or vortex core sizes. Additionally, it is unlikely that there would be serious issues regarding structural modifications and fatigue because this wake alleviation concept operates by decreasing the wing's outboard loading, which generates a smaller bending moment in the wing.

The second advantage of the notched-ogee concept is that it has the potential to allow the development of rapidly growing instabilities by delaying the merging of the tip and flap vortical structures. The extensive delay in the merger could be beneficial in inducing short and long wave instability modes, which may hasten the onset of vortex breakdown by changing the two-dimensional nature of the wake into a three-dimensional one. The resulting incoherent wake would pose less of a threat to a following aircraft. Thus, these novel wing designs appear worthy of more detailed investigations.

VI. Conclusions

Numerical simulations of trailing wakes induced by swept-notched ogee/triangular wings have been undertaken using computational fluid dynamics. Initially, the applicability of CFD to the simulations of rectangular wing wakes was investigated via comparisons with experimental data [13,14]. The results [15–17] demonstrated the ability of the RANS equations to reproduce the global topology of trailing wakes as they evolve downstream; vortex characteristics were found to be consistent with the experimental vortex properties. Numerical simulations were then performed for the present sets of wing geometries. The novel swept wings combined triangular and ogee wing-tip sections with the original notched design at various locations along the span. The wake

properties and characteristics acquired were evaluated against the reference wing models, models 1 (swept conventional) and 2 (swept notched), by comparing the vorticity plots, core separation distances, circulations, and induced rolling moments.

By modelling the wing-tip sections from 75 to 87%s, it has been observed that the behavior and structure of the wake is widely altered. The wake structures of the swept wings defined in sets 1 and 2 are noticeably dependant on wing-tip section geometries, spanwise locations, and elapsed distances from the trailing edge. Two distinctive wake evolutions are distinguished throughout the measurements; unsurprisingly, the dipole structure of the swept conventional wing (model 1) merges, whereas the initial tripole and quadrupole vortical structures of the swept-notched wing (model 2) and the wing models tested in set 2 (wing-tip sections modeled at 50%c and 75, 80, and 87%s) stay visibly apart with no merger occurring by 24s. In addition, two merger processes are observed between the addition vortex and the tip vortices. These observations are confirmed in light of additional data in two ways: the core separation distances are reduced when compared with reference wing model 2 (swept notched), and an inboard shift towards the center of the wing is observed in the overall centroid locations. Over the entire range of swept-notched wings examined, one finds a reduction in the separation distance associated with lower wing-tip section spanwise locations (from 100 to 75%s). Significant reductions in individual and total circulations, and induced rolling moment, are observed when the novel swept-notched wings (set 2) are used in place of the reference wings (models 1 and 2). All individual and total circulations values given by the wing models defined in set 2 are reduced when compared with the reference wing model 2 (swept notched) at all measurement planes; average reductions up to 20% are recorded for the tip and total circulations data. The mean lowest tip and total circulations are obtained with the triangular and ogee wing-tip sections located at 75%s [models 3 (SN50Tri75) and 4 (SN50Sik75)]. Furthermore, the resulting distributions of induced rolling moment obtained with the novel swept wings are drastically reduced when compared with those in the wake of the swept conventional and swept-notched wings (models 1 and 2). The novel swept wings show up to 33 and 45% lower C_M*/C_L values when compared with the swept-notched wing (model 2) and the swept conventional wing (model 1), respectively. This would therefore imply that an aircraft with an optimum-notched ogee/triangular design could be made 45% heavier than one with a conventional high-lift concept without a wake vortex hazard penalty.

It can be stated that different wing geometries lead to different wake structures and properties, and that all of the novel swept wings shown in this paper have the negative vorticity characteristic; indeed, all represent an improvement on conventional high-lift distribution. Beyond the apparent point that the wing-tip sections located at 75%s are the optimum designs in reducing the far-wake strength, the ogee wing-tip section located at 80%s [model 5 (SN50Sik80)] appears to be the best compromise and the most effective of the wing designs, because it produces substantial high vortex spacing with relatively low vortex strength and induced rolling moment values at far-field regions.

To conclude, the importance of wing geometries in the minimization of the trailing wake has been demonstrated and the data have undoubtedly indicated that swept-notched ogee/triangular wings offer a promising avenue for an effective wake hazard reduction. One is therefore led to consider a more effective design for the reduction of the complex wake phenomenon; further investigations for swept-notched wing designs will include various spanwise locations for the notch geometry and the testing of twin notches at several spanwise locations. This will form the basis of future publications.

Acknowledgments

The authors would like to acknowledge W. R. Graham and S. W. Park for their active assistance in providing experimental data resources and many fruitful discussions.

References

[1] Gerz, T., Holzapfel, F., and Darracq, D., "Aircraft Wake Vortices—A Position Paper," *5th WakeNet Workshop on Wake Turbulence and the Airport Environment*, CERFAC, Paris, April 2001, pp. 1–43.

[2] Hunecke, K., "Wake Vortex Control—A Challenge for Large Transport Aircraft," *Air & Space Europe*, Vol. 3, No. 3, May 2001, pp. 209–213. doi:10.1016/S1290-0958(01)90097-8

[3] Chambers, J. R., "Concept to Reality: Contributions of the NASA Langley Research Center to U. S. Civil Aircraft of the 1990s," NASA History Series, NASA SP-2003-4529, 15 Dec. 2002.

[4] Graham, W. R., Bertény, T., and David, L., "The Effect of Flap-End Additions on Aircraft Trailing Vortices," *The Aeronautical Journal*, Vol. 108, Feb. 2004, pp. 109–115.

[5] Arguelles, P., "European Aeronautics: A Vision for 2020," Jan. 2001, pp. 1–26.

[6] Lee, G. H., "Trailing Vortex Wakes," *The Aeronautical Journal*, Vol. 79, No. 271, Sept. 1975, pp. 377–388.

[7] Kirkman, K., Brown, L., Clinton, D., and Goodman, A., "Evaluation of Effectiveness of Various Devices for Attenuation of Trailing Vortices Based on Model Tests in a Large Towing Basin," NASA CR-2202, Dec. 1973.

[8] Rossow, V. J., "Lift-Generated Vortex Wakes of Subsonic Transport Aircraft," *Progress in Aerospace Sciences*, Vol. 35, No. 6, 1999, pp. 507–660. doi:10.1016/S0376-0421(99)00006-8

[9] Glauert, H., *The Elements of Aerofoil and Airscrew Theory*, 2nd ed., Cambridge Univ. Press, Cambridge, England, U.K. 1947, Chap. 10.

[10] Rossow, V. J., "Theoretical Study of Lift-Generated Vortex Wakes Designed to Avoid Roll-Up," *AIAA Journal*, Vol. 13, No. 4, 1975, pp. 476–484.

[11] Donaldson, C. duP., and Sullivan, R. D., "Decay of an Isolated Vortex," *Aircraft Wake Turbulence and Its Detection*, 1st ed., edited by J. H. Olsen, A. Goldburg, and M. Rogers, Plenum, New York, 1971, pp. 389–411.

[12] Graham, W. R., "Optimising Wing Lift Distribution to Minimise Wake Vortex Hazard," *The Aeronautical Journal*, Vol. 106, Part 1062, Aug. 2002, pp. 413–426.

[13] Graham, W. R., Park, S. W., and Nickels, T. B., "Trailing Vortices from a Wing with a Notched Lift Distribution," *AIAA Journal*, Vol. 41, No. 9, 2003, pp. 1835–1843.

[14] Park, S. W., "Study into the Merger of Co-Rotating Wing Tip and Flap Vortices," Ph. D. Thesis, Univ. of Cambridge, Cambridge, England, U.K., 2005.

[15] Szkatula, L., Zouaoui, Z., and Yang, X., "Computational Analysis of Wake Vortices Generated by a Notched Wing," AIAA Paper 2006-0245, 9–12 Jan. 2006.

[16] Zouaoui, Z., Szkatula, L., and Grant, R. J., "Computational Analysis of Wake Vortices Generated by Notched Wings," *Journal of Aircraft*, Vol. 44, No. 2, 2007, pp. 487–500. doi:10.2514/1.23918

[17] Szkatula, L., "Analysis of the Vortical Flow Dynamics Induced by Notched Wing Designs for Wake Hazard Alleviation," Ph. D. Thesis, Univ. of Wales, Wales, U.K., 2007.

[18] Choudhury, D., "Introduction to the Renormalization Group Method and Turbulence Modelling," Fluent, Inc., TM TM-107, 1993, pp. 1–61.

[19] Yakhot, V., and Orszag, S. A., "Renormalization Group Analysis of Turbulence: 1. Basic Theory," *Journal of Scientific Computing*, Vol. 1, No. 1, 1986, pp. 3–51. doi:10.1007/BF01061452

[20] Lund, T., "Application of the Algebraic RNG Model for Transition Simulation," *Instability, Transition, and Turbulence*, edited by M. Y. Hussaini, A. Kumar, and C. L. Streett, Springler–Verlag, Berlin/New York/Heidelberg, 1992.

[21] Cerretelli, C., and Williamson, C. H. K., "The Physical Mechanism for Merging of Trailing Vortices," *Journal of Fluid Mechanics*, Vol. 475, No. 1, Jan. 2003, pp. 41–77. doi:10.1017/S0022112002002847

[22] Leweke, T., Meunier, P., Laporte, F., and Darracq, D., "Controlled Interaction of Co-Rotating Vortices," *3rd ONERA–DLR Aerospace Symposium*, ONERA, Paris, June 2001.

[23] Chen, A. L., Jacob, J. D., and Savas, O., "Dynamics of Corotating Vortex Pairs in the Wakes of Flapped Airfoils," *Journal of Fluid Mechanics*, Vol 382, 1999, pp. 155–193. doi:10.1017/S0022112098003814